J|A|C|S
JOURNAL OF THE AMERICAN CHEMICAL SOCIETY

pubs.acs.org/JACS

Article

Responsive Plasmonic Reporters Decrypt Nanoparticle-Induced Single Membrane Protein Degradation

Jin Wang, Jing Tan, Zhao Zhang, Xiuxiu Wang, Jing Zhao, Jie Li, and Chen Wang*

Cite This: J. Am. Chem. Soc. 2025, 147, 38549−38561

Read Online

ACCESS | Metrics & More | Article Recommendations | SI Supporting Information

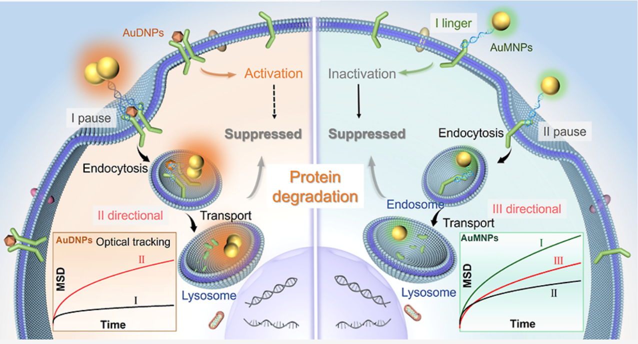

ABSTRACT: Nanoparticle-mediated degradation of proteins of interest has recently emerged as a powerful tool in biomedical research and the pharmaceutical industry. Nevertheless, the limited understanding of dynamic processes poses challenges in further improving the efficacy. Herein, we develop responsive plasmonic nanoprobe systems capable of discrimination between membrane protein monomer and dimerization states, enabling the direct observation of membrane protein degradation during nanoparticle endocytosis. The nanoprobes are engineered with precisely controlled aptamer modifications through asymmetric spherical nucleic acid functionalization to ensure low-valence protein binding. Upon ligand stimulation, protein dimerization triggers proximity-induced DNA hybridization between nanoprobe and protein complexes, resulting in distinctive plasmonic coupling signals. Using the cellular mesenchymal to epithelial transition factor (Met) as a model protein, we demonstrate differential endocytosis kinetics between monomeric and dimeric states, with dimers exhibiting enhanced endocytic efficiency. Further investigation into downstream protein expression and cellular responses reveals an enhanced phosphorylated Met (p-Met) degradation process by the aggregation state, providing insights into the relationship between protein oligomerization and nanoparticle-mediated degradation efficiency. These findings offer valuable theoretical foundations for designing targeted protein degradation platforms based on nanoparticles.

■ INTRODUCTION

Targeted protein degradation (TPD) technology has emerged as a powerful approach for selective protein elimination through intracellular recycling mechanisms, garnering significant attention over the past two decades.[1] Commonly, TPD methods promote protein degradation mainly by targeting protein hydrolysis chimeras (PROTACs), autophagy-lysosome mechanism, etc.[2−4] However, most of these TPD platforms are designed primarily for the cytoplasmic proteins. To achieve targeted degradation of non-cytoplasmic targets, lysosome-targeted chimeras (LYTACs) were developed,[5] which bind and transport proteins of interest on the cellular membrane or extracellularly into the lysosome.[6] Currently developed LYTAC platforms typically employ bifunctional molecules that ligate the extracellular structural domains of target proteins to lysosomal transport receptors (LTRs), thereby triggering endocytosis and subsequent lysosomal degradation.[7] Although these approaches have shown promise, their reliance on specific receptors, complex design requirements, and laborious modification processes substantially constrains their expandability.[2,8]

Biocompatible nanomaterials, including noble metal nanoparticles, nanoporous materials, polymer nanoparticles, etc., demonstrate efficient cellular internalization.[9,10] Their structural flexibility and facile surface modification capabilities make them promising candidates for developing multifunctional TPD tools.[11,12] Studies have revealed that engineered nanoparticles can undergo cellular uptake and endosomal trafficking, without requiring specific receptors to facilitate cell entry and lysosomal-directed targeting.[13] Recent breakthrough work by Shi and colleagues demonstrated that nanoparticles can facilitate receptor-independent protein internalization, with applicability to a wide range of targets and different nanoparticle types.[14] More recently, Zhang's group developed a customizable aptamer-nanoparticle-assisted targeted degradation technique that utilizes a clathrin-mediated pathway to achieve highly efficient endocytosis and precise lysosomal degradation of several membrane proteins.[15] These novel platforms significantly circumvent the reliance on endogenous LTRs and the resulting risk of a potential off-target effect of the conventional strategy. This nanoparticle-mediated TPD technology established a universal strategy for

Received: July 19, 2025
Revised: October 8, 2025
Accepted: October 9, 2025
Published: October 14, 2025

Scheme 1. Schematic Diagram of the Nanoparticle-Induced Membrane Protein Degradation Processes in the Monomer State (Right) and the Activated Dimer State (Left)

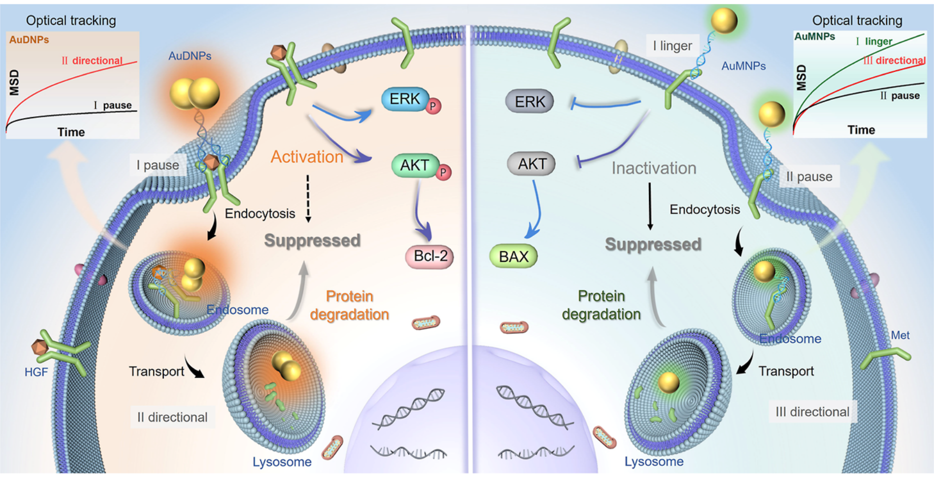

targeted extracellular protein degradation, promising to change the cumbersome development of existing TPD tools.[4] Despite these advances in nanoparticle-based TPD development, current strategies for validating the effectiveness of TPD platforms are mostly limited to end point measurements such as protein expression levels.[16] Direct probing of the particle−cell interaction and endocytosis pathway is still lacking.[17] A comprehensive understanding of these spatiotemporal dynamics would enhance our knowledge of cellular signaling processes and ultimately improve TPD efficiency.[18,19]

With the rapid development of optical microscopy, single-particle tracking (SPT) has been widely studied in recent years as a powerful means for directly characterizing individual particle dynamics at high precision.[20−22] It enables real-time monitoring of spatiotemporal motion trajectories, providing crucial insights into nanostructure−protein dynamics and subsequent intracellular signaling cascades.[23,24] Recently, He's group revealed unprecedented details of ErbB receptor dynamics at the nanoscale, marking a significant advance in understanding membrane protein trafficking.[25] Current studies predominantly employ densely ligand-modified nanoparticles to investigate the protein endocytosis process. However, this approach presents inherent limitations, particularly for membrane proteins like growth factor receptors, where ligand binding triggers activation and internalization.[26,27] The degradation efficiency and downstream signaling may vary significantly between monomeric and dimeric receptor states.[28] This underscores the critical need for advanced nanoprobes capable of monitoring nanoparticle-mediated protein degradation across different aggregation states, which is essential for evaluating the TPD efficacy.

Herein, we present plasmonic nanoprobe AuMNPs capable of efficiently distinguishing between membrane protein monomer and dimerization states, facilitating direct observation of the membrane protein degradation processes mediated by nanoparticle endocytosis. Leveraging the precisely controlled low-density modification of specific aptamers, the prepared AuMNPs achieve a low-valency binding to individual membrane proteins. When natural ligands induce protein dimerization, AuMNPs bound to Met will form a dimer structure (termed AuDNPs) due to proximity-induced DNA hybridization, leading to significantly different localized surface plasmon resonance signals. This allows for the discrimination of proteins in different aggregation states. As a proof of concept, we tracked the nanoparticle-mediated endocytosis dynamics of the cellular mesenchymal to epithelial transition factor (Met) protein in both monomeric and dimeric states, revealing that the motility behaviors in the two states differ significantly (Scheme 1). Specifically, the endocytosis efficiency of monomers is lower than that of the dimers. Additionally, we observed distinct degradation efficiencies between different protein states and elucidated the underlying mechanisms through cellular morphological and behavioral analyses. These results provide valuable insights for designing TPD platforms based on nanoparticles.

■ RESULTS AND DISCUSSION

Design and Characterization of the Responsive Plasmonic Reporters for Protein Imaging on Living Cells. To achieve precise protein recognition and membrane binding, DNA aptamer-containing nucleic acid probes have been employed. As a proof of concept, the receptor tyrosine kinase Met was selected as a model target protein.[29] Previous studies have demonstrated that Met is activated upon binding with its native ligand, hepatocyte growth factor (HGF), which induces protein dimerization.[30] A nucleic acid sequence containing the oligonucleotide-based mimetics of HGF (denoted as SL1) was selected as the recognition molecule.[31] Additionally, a complementary sequence of Met recognition probes is designed to characterize the dimerization state by the proximity-induced DNA assembly (Figures S1 and S2).[32] Then, we investigated these DNA probes for analyzing Met dimerization on living cell membranes. As shown in Figures 1A and S3 and S4, after incubating the fluorescein (FAM)-modified DNA probes with Met-overexpressing MDA-MB-231 and A549 cells for 15 min, intense fluorescence signals appeared on the cell surface by confocal laser scanning microscopy (CLSM). In contrast, fluorescence was relatively weak in Met-low-expressing MCF-10A cells (Figure S5). In the presence of HGF, a negligible fluorescence signal of FAM was observed, indicating that the proposed approach is capable of imaging ligand-induced receptor dimerization (Figure S6). The results obtained from flow cytometry analysis corroborated those observed in the CLSM images (Figure S7).

Nanoparticles bound to the cell membrane tend to be internalized into cells by receptor-mediated endocytosis.[10] To

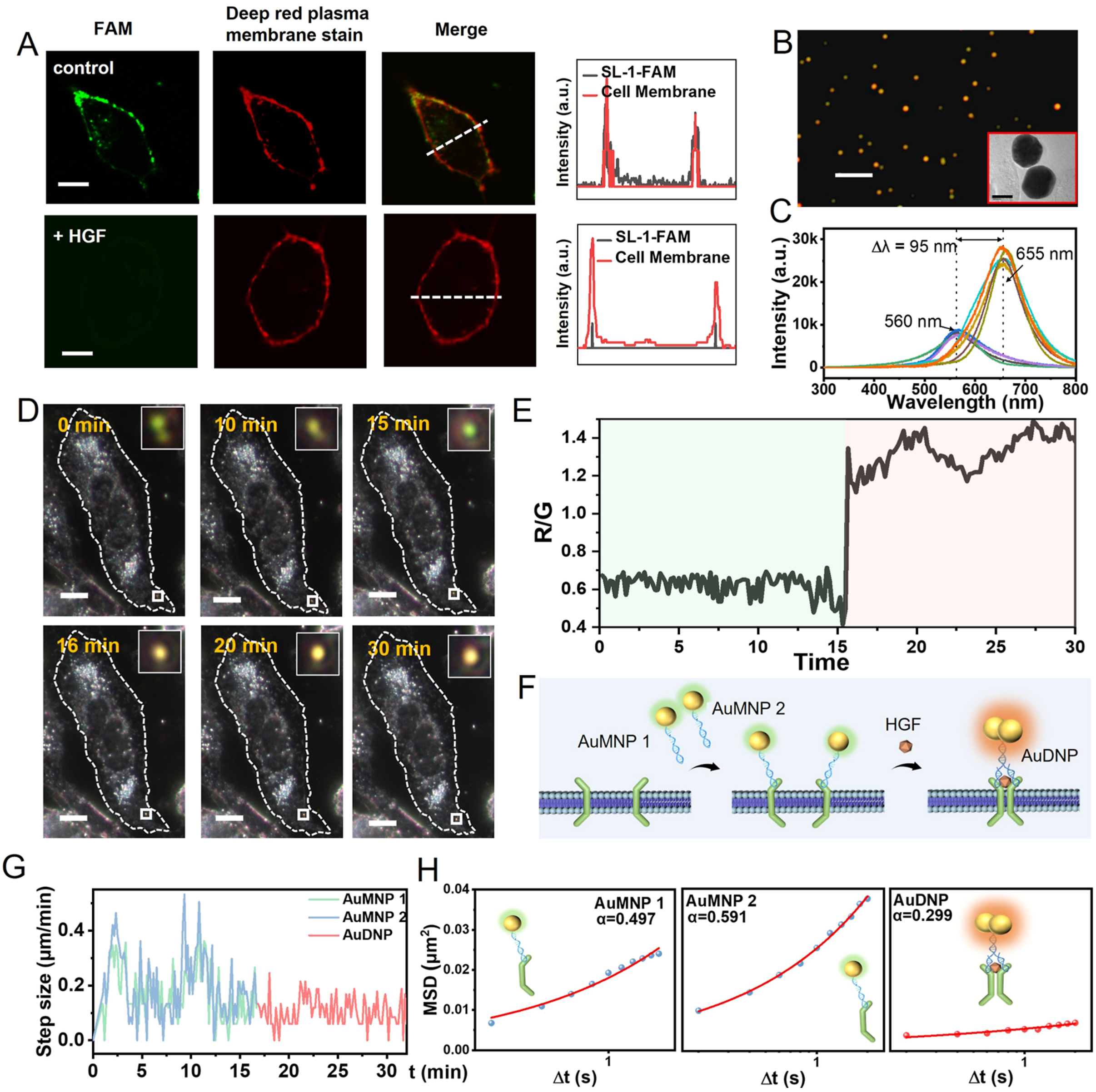

Figure 1. Characterization of the responsive plasmonic reporters for Met protein imaging on living cells. (A) Confocal imaging of MDA-MB-231 cells incubated with SL1-A-FAM (green channel), SL1-B-BHQ1, and DeepRed plasma membrane dyes (red channel) with and without HGF. Scale bar: 10 μm. Spectra were obtained by profiling the fluorescence intensity of FAM and cell membrane dye along the white dotted line in the merge channel. (B) DFM image of AuDNPs. Scale bar: 10 μm. Inset: High-resolution transmission electron microscopy (HRTEM) image of a single AuDNP. Scale bar: 50 nm. (C) Typical single-particle scattering spectra of AuMNPs and AuDNPs. (D) Real-time DFM images of living HeLa cells incubated with AuMNPs in the presence of HGF. Inset: the enlarged images in the white box. Scale bar: 10 μm. (E) The scattering signal changes of the enlarged nanoparticle in (D) over time. (F) Schematic illustration of the in situ assembly process of AuMNPs on the cell membrane in the presence of HGF. (G) Time series of the step size of AuMNPs and AuDNPs. (H) Plot of mean square displacement (MSD) versus time interval.

investigate the nanoparticle-mediated endocytosis process, gold nanoparticles (AuNPs) modified with aptamers were chosen as probes for real-time tracking, given their good stability, ease of modification, and unique optical properties.[33,34] First, AuNPs with an average diameter of ~76 nm were prepared, which displayed green scattering light under dark-field microscopy (DFM, Figure S8). To achieve low-valency targeting of membrane proteins, DNA aptamers were asymmetrically conjugated to polyethylene glycol (PEG)-functionalized gold nanoparticles (AuNPs) using a previously established modification strategy.[23,35] The obtained nanoprobes (termed AuMNP) were characterized and quantified by UV−vis absorption spectroscopy (Figures S9 and S10). AuMNPs exhibited an ultralow aptamer valency, with an arsenal of ~7.6 DNA strands per particle (Figure S11), thereby enabling targeted protein engagement with minimal multivalency effects.

To effectively distinguish between monomeric and dimeric states of membrane proteins, we further introduced an in situ DNA assembly strategy for labeling and imaging of protein dimers by proximity-induced DNA hybridization in the presence of a ligand. The assembled nanodimer (denoted as AuDNPs) displayed characteristic scattering spectra distinct from AuMNPs, exhibiting a 95 nm redshift due to plasmonic coupling (Figures 1B,C, and S12). Compared to conventional spherical nucleic acids, the asymmetric modification strategy

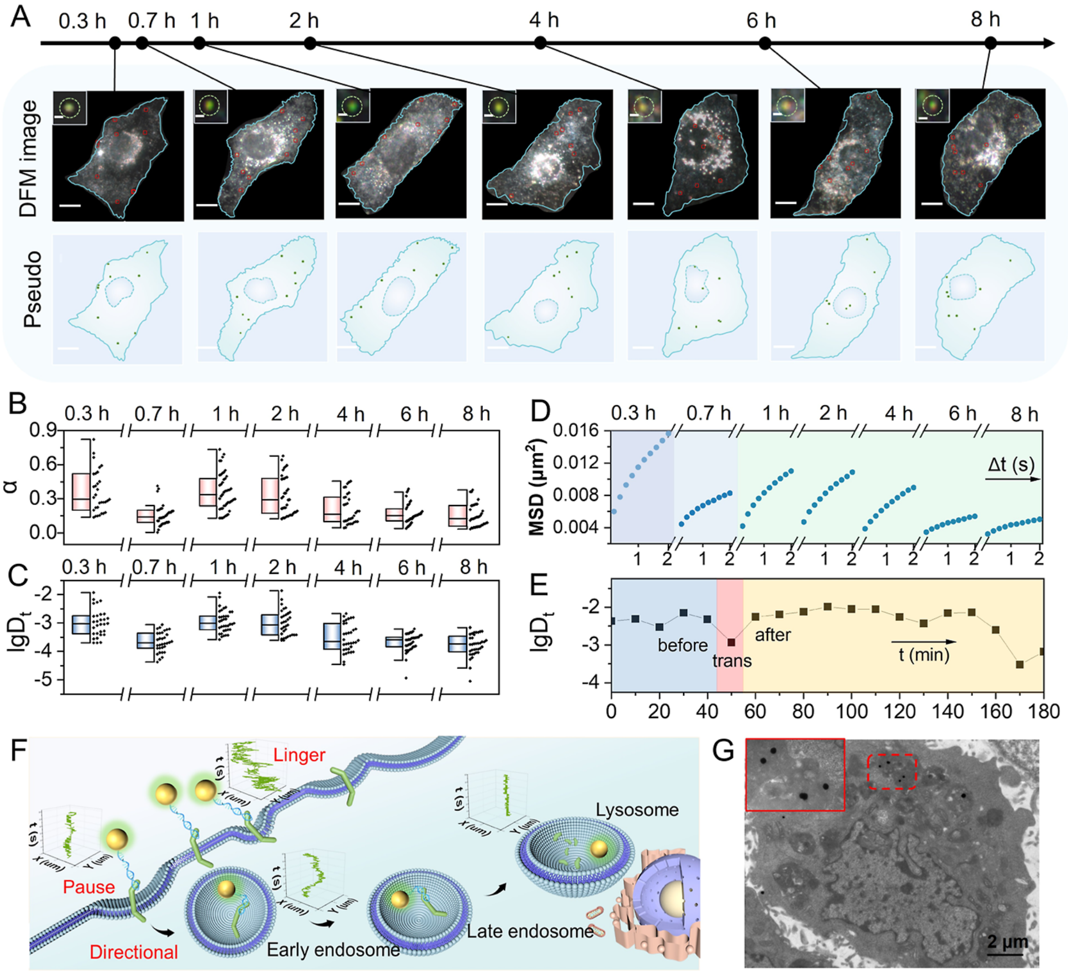

Figure 2. Direct observation of the Met degradation process via cellular tracking of AuMNPs. (A) DFM images of MDA-MB-231 cells after being incubated with AuMNPs for different times. The red circles indicate endocytosed AuMNPs. Inset: enlarged image of the typical nanoparticles in cells. Scale bar: 10 and 1 μm (insert). (B,C) Distributions of the diffusion exponent (B) and D_t (C) of AuMNPs in living cells after being incubated for different times. (D) The average MSD of AuMNPs in living cells after being incubated for different times. (E) The time series D_t of a single AuMNP extracted from the real-time DFM monitoring. (F) Schematic illustration of the endocytosis dynamics of AuMNPs. According to the characteristic dynamic of AuMNPs in cells at different times, the cellular uptake of AuMNPs was divided into three stages. Linger: landing on the plasma membrane; pause: captured and encapsulated by the nascent vesicles; directional: diffused in the cytoplasm toward the nucleus, eventually confined in the crowded perinucleus. (G) TEM image of the MDA-MB-231 cell after being treated with AuMNPs. Inset: the enlarged image in the red dashed box.

significantly enhanced the dimer formation efficiency (>30%, Figures S13 and S14). Dynamic light scattering experiments further confirmed the successful assembly of dimers in solution (Figure S15). HRTEM revealed that the average interparticle distance of the dimer was about 3.2 nm (Figure S16). We also simulated the scattering spectra of AuMDPs with different spacings using the finite-difference time-domain method, which was found to be consistent with our measured results (Figures S17 and S18). Additionally, both AuMNPs and AuDNPs probes maintained good stability and biocompatibility in the cell culture environment, revealing their excellent potential in biomedical applications (Figures S19−S21). Remarkably, even when dispersed in serum, the scattering signals of these nanoprobes remained unchanged for 24 h (Figure S22). We attribute this stability primarily to the dense PEG coating on the nanoparticle surface, which was hypothesized to reduce nonspecific protein adsorption and preserve aptamer functionality,[36] making it encouraging for future in vivo applications.

Inspired by the results presented above, we further investigated the feasibility of the probes in targeting and imaging living cells. As shown in Figure S23, the number of AuMNPs bound to the surface of MDA-MB-231 cells was significantly higher than that of nontargeted nanoparticles under the same conditions. To investigate membrane protein dynamics, we implemented SPT, a powerful technique for resolving spatiotemporal heterogeneity in complex cellular environments.[37] Following HGF stimulation, we observed in situ assembly of AuDNP on the cell membrane (Figure 1D). The monomer-to-dimer transition occurred within approximately 16 min, as evidenced by a clear scattering signal shift through time-resolved R/G signal analysis (Figure 1E). This striking shift offers a high signal-to-noise performance for tracking individual protein dynamics (Figure 1F). Trajectory analysis of a representative nanoparticle revealed markedly reduced mobility following dimerization (Figure 1G), indicating a protein dimerization event. To quantitatively characterize these dynamic transitions, we performed MSD analysis (methodological details in the Supporting Information). As

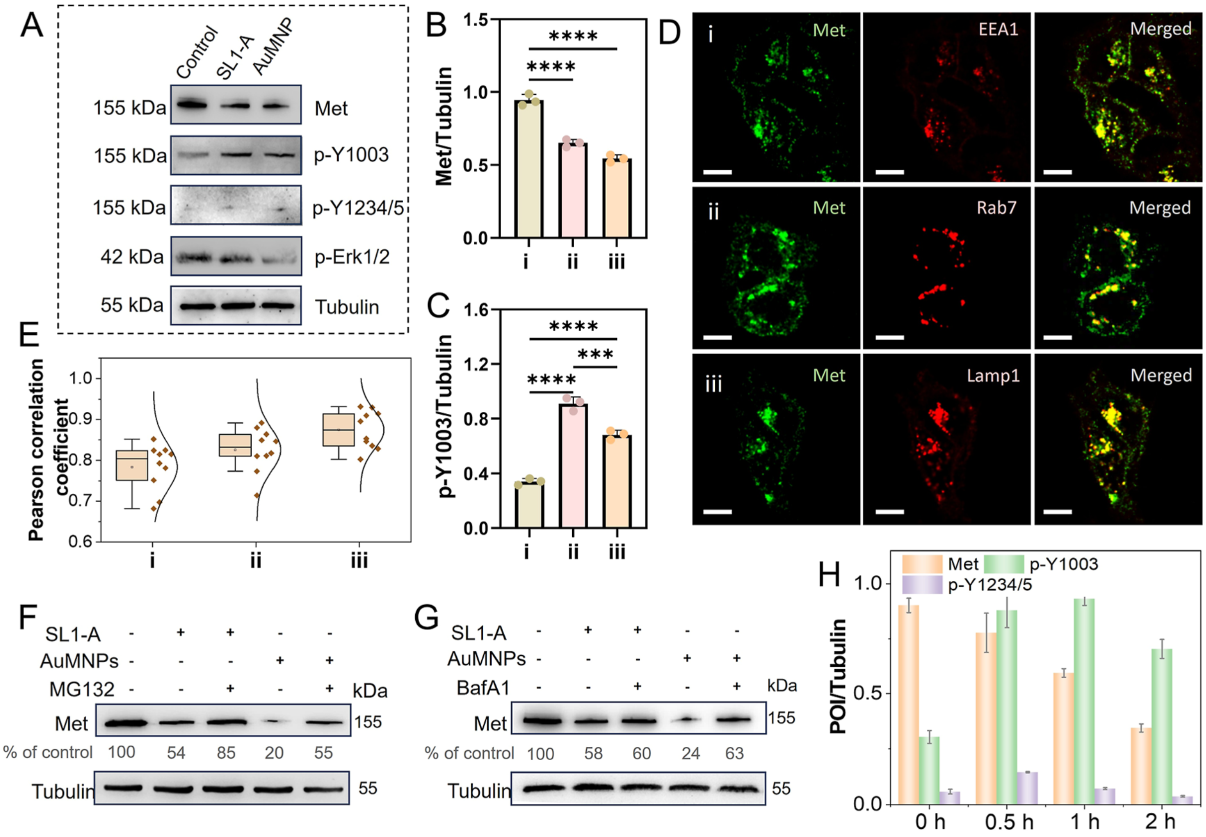

Figure 3. Analysis of the mechanism of Met degradation triggered by AuMNPs endocytosis. (A) Western blot (WB) analysis of Met, Met phosphorylation, and Erk1/2 phosphorylation after different treatments. (B,C) Statistics of the level of Met (B) and phosphorylation of Met at Y1003 (C) after different treatments (i: control, ii: SL1 treated, iii: AuMNPs treated). (D) Confocal microscopy imaging of internalized Met (green) and mCherry-labeled EEA1/Rab7/Lamp1 (red). Cells were pretreated under different conditions: (i) transferred with a plasmid encoding mcherry-EEA1 for 36 h, followed by treated with AuMNPs for 1 h; (ii) transferred with a plasmid encoding mcherry-Rab7 for 36 h, followed by treated with AuMNPs for 2 h; (iii) transferred with a plasmid encoding mcherry-Lamp1 for 36 h, followed by treated with AuMNPs for 4 h. Then the Met was immunofluorescence stained and imaged in each group. Scale bar: 10 μm. (E) Pearson correlation analysis of Met colocalization with endolysosomal markers under different treatments in (D). (F,G) The effect of proteasome inhibitor MG132 (F) or lysosome inhibitor Baf1A (G) on Met degradation triggered by SL1-A or AuMNPs, as determined by c-Met levels. (H) Statistics of the level of Met and Met phosphorylation after treatment for different times.

illustrated in Figure 1H, the MSD analysis of trajectories revealed that AuMNPs initially exhibited a weakly confined diffusion on the cell membrane with diffusion exponents (α) ranging from 0.5−0.6. Following protein dimerization, the motion transitioned to a more confined state, featuring a significantly reduced diffusion exponent ($\alpha \sim 0.3$). Through quantitative analysis of dimer formation efficiency on the cell surface after HGF stimulation, we observed a yield of up to 47%, significantly higher than that achieved via solution-phase self-assembly (Figure S24). This enhancement is likely due to a proximity-induced hybridization effect resulting from HGF-promoted Met dimerization.[32] These results collectively establish our responsive plasmonic reporters as a robust platform for real-time monitoring and discrimination of protein monomer−dimer transitions.

Direct Observation of the Met Degradation Process via Cellular Tracking of AuMNPs. After confirming that the probes could distinguish between proteins in the monomeric and dimerized states, we first investigated the endocytosis dynamics of Met monomers using AuMNPs. As illustrated in Figure S25, the scattered light of a single AuMNP bound to the cell membrane appeared green under DFM, consistent with the signal of the phosphorus dispersed in the culture medium. Extended coincubation periods with living cells increase the adsorption of biomolecules onto nanoparticle surfaces, leading to more complex cell−particle interactions.[17] Accordingly, we initiated single-particle endocytosis monitoring when adequate AuMNPs diffused near the cell membrane. This process typically commenced after 10 min of incubation with MDA-MB-231 cells, by which time nearly all membrane-bound nanoparticles are present in a monomeric state. Guided by established endocytosis mechanisms,[38] we systematically tracked seven batches of cells that were incubated with cells for 0.3, 0.7, 1, 2, 4, 6, and 8 h, respectively, analyzing ∼40 randomly selected trajectories from 5 to 8 viable cells per group. As shown in the DFM images, many bright green dots representing AuMNPs were initially dispersed at the plasma membrane and subsequently accumulated around the nuclear periphery during the prolonged incubation (Figure 2A).

Quantitative analysis of AuMNPs trajectories showed distinct motion patterns that could be classified into three categories based on their confinement degrees: weakly confined (linger), severely confined (pause), and directional. Specifically, as displayed in Figures 2B,C, following 0.3 h of coincubation with cells, AuMNPs specifically recognized the extracellular structural domain of Met protein and bound to the cell membrane. The X−Y trajectory analysis revealed weakly confined motion of AuMNPs on the membrane, characterized by a relatively high diffusion exponent and coefficient ($\alpha = 0.423$, $D_t = 0.00195$). At 0.7 h, trajectory and displacement analyses demonstrated predominantly severe confined motion, with significantly reduced diffusion parameters ($\alpha = 0.274$, $D_t = 0.000813$), suggesting AuMNPs entrapment within membrane-derived vesicles during early endocytosis (Figures S26−S28). Subsequently, the velocity, α, D_t, and displacement of AuMNPs displayed an increasing trend, which signified that Met-bound AuMNPs began to enter the cell through early endosomes (Figures S29−S32).[9] DFM imaging indicated that intracellular motion peaked at 2 h, with reduced confinement ($\alpha = 0.372$, $D_t = 0.00125$) and directional movement toward the nucleus (Figure 2D). As most of the AuMNPs had been transported to the more crowded perinuclear region (after 4 h), the motion confinement gradually increased (Figure S33). After 8 h of incubation, the AuMNPs were mostly "sluggish" in the perinuclear area, and the diffusion exponent decreased to ∼0.2. Notably, a subset of AuMNPs maintained significant motility outside the perinuclear region (Figures 2A and S34). Given that aptamer-targeted Met undergoes Y-1003 phosphorylation-induced protease degradation,[39] we hypothesize that these anomalous trajectories reflect AuMNP detachment due to Met degradation, disrupting receptor-mediated endocytosis. Similar phenomena were also observed in Met-positive A549 cells, confirming the universality of AuMNP nanoprobes for monitoring the Met degradation process (Figure S35).

To comprehensively investigate the dynamic endocytosis process of AuMNPs, we tracked the intracellular movement patterns of a single AuMNP over a 3 h period. Following a 10 min incubation with AuMNPs, cells were transferred from the incubator for microscopic trajectory analysis. The results revealed that AuMNPs exhibited significant spatial restriction at approximately 50 min postincubation, followed by cellular internalization via endocytosis. Detailed trajectory analysis before and after endocytosis demonstrated that the diffusion exponent first decreased to 0.0828, subsequently increasing to 0.447 (Figure S36). The temporal changes in D_t values obtained from SPT aligned well with the observed dynamics of the Met monomer mobility at different time points (Figure 2E, F). Additionally, TEM imaging after 2 h of incubation revealed well-dispersed AuMNPs within the cytoplasm, confirming successful cellular uptake (Figure 2G).

The Mechanism of Met Degradation through Aptamer-Modified AuMNPs. To further validate the nanoparticle-mediated Met endocytosis efficiency, we used 80 nm fluorescence SiO_2 nanoparticles with the same modification procedures as an alternative to AuMNPs. The CLSM images showed progressive internalization of FAM-labeled nanoparticles, demonstrating their transition from initial plasma membrane localization to subsequent cytoplasmic accumulation over extended incubation periods (Figures S37 and S38). Moreover, immunofluorescence analysis revealed a time-dependent reduction in the Met level (Figure S39). Specifically, significant decreases in membrane-localized Met were observed at 0.5, 2, and 6 h post-nanoparticle treatment. These temporal dynamics provide strong experimental validation for the nanoparticle-induced membrane protein degradation.

To elucidate the molecular mechanism underlying Met degradation, we examined both total Met expression and site-specific phosphorylation using antibodies targeting Y1003 and Y1234/5 residues in MDA-MB-231 and A549 cells after different treatments (Table S2). Although both free aptamer and AuMNPs induced Met degradation, AuMNPs exhibited enhanced degradation efficiency (Figures 3A,B and S40). Cellular protein degradation typically proceeds through either the ubiquitin-proteasome system or the lysosomal pathway.[2] Previous studies have shown that Met-specific aptamers trigger degradation through selective phosphorylation at Y1003 in the juxtamembrane domain rather than Y1234/5 in the kinase domain.[39] Consistent with these findings, we observed significant Y1003 phosphorylation but minimal Y1234/5 phosphorylation in MDA-MB-231 cells after 2 h of treatment with either aptamer or AuMNPs (Figure 3A,C). These results support the hypothesis that low-valency targeted AuMNPs effectively bind monomeric Met without inducing multivalent aggregation. Interestingly, the level of Y1003 phosphorylation was slightly lower in the AuMNP-treated group than in the aptamer group, which we hypothesized was attributed to nanoparticle-mediated endocytosis.

We also performed colocalization studies to track the internalization and trafficking of Met following AuMNP treatment. After 1 h of stimulation, Met exhibited strong colocalization with the early endosome marker EEA1 and subsequently translocated to Rab7-positive late endosomes (Figure 3D). Within 4 h, Met levels were markedly reduced and showed high colocalization with Lamp1-positive lysosomes, supporting efficient lysosomal degradation (Figure 3E). Surface biotinylation experiments were conducted to further validate the endocytic pathway of AuMNPs. The results showed a remarkable decrease in Met level on the cell surface, confirming that internalized Met was not recycled but degraded in lysosomes under these conditions (Figure S41). To further validate the protein degradation pathways, MDA-MB-231 cells were treated with AuMNPs or SL1-A in the presence of the proteasome inhibitor MG132 or the lysosome inhibitor bafilomycin A1 (BafA1).[40,41] As shown in Figure 3F, MG132 inhibited the degradation effects of both SL1-A and AuMNPs, with a weaker inhibitory effect on AuMNPs. In contrast, BafA1 significantly impaired AuMNP-induced degradation but had no effect on SL1-A-mediated degradation (Figure 3G). These results indicate that AuMNP-induced degradation involves both proteasomal and lysosomal pathways, whereas SL1-A relies primarily on the ubiquitin−proteasome system. To validate this deduction, we constructed AuMNPs functionalized with a fibroblast growth factor receptor (FGFR)-specific aptamer (AuMNPs-F), which has been reported not to trigger proteasomal degradation.[42] As shown in Figure S42, AuMNPs-F treatment resulted in a marked reduction in FGFR levels, and this degradation was inhibited only by BafA1, confirming a lysosome-dependent mechanism without proteasomal involvement. Following confirmation of the efficient protein degradation induced by AuMNPs, we also assessed Met mRNA expression levels under different treatments and observed no significant changes (Figure S43).

To elucidate the synergistic mechanism by which aptamers and nanoparticles promote Met degradation, we conducted a time-course analysis of Met phosphorylation at the Y1003 and Y1234/5 sites following AuMNP treatment. The results revealed that the phosphorylation level of Y1003 gradually increased within the first hour of aptamer binding, followed by a subsequent decline (Figure 3H). Combined with the results of endocytosis dynamics of AuMNPs in Figure 2, it can be inferred that the reduction in the phosphorylation level of Y-

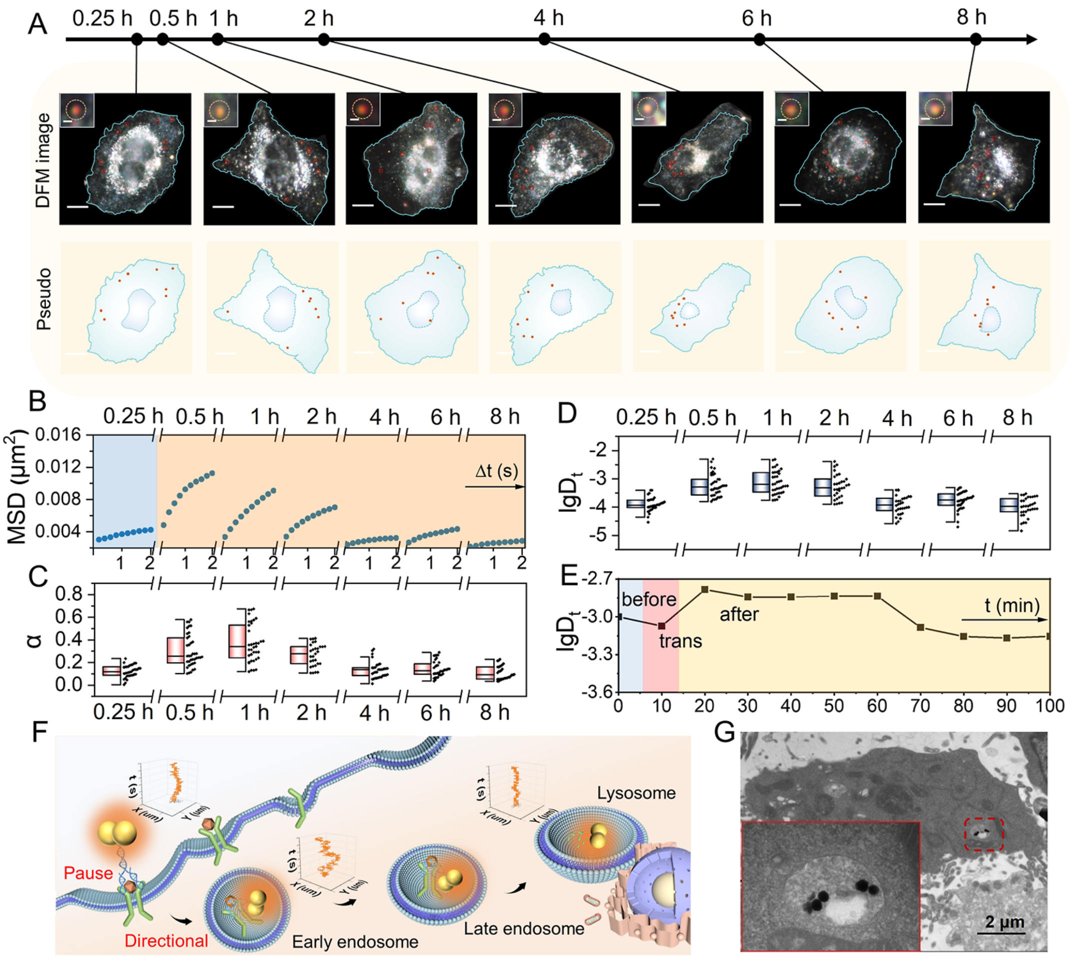

Figure 4. Direct observation of the p-Met degradation process via cellular tracking of the in situ assembled AuDNPs. (A) Representative DFM images and corresponding annotated images of AuDNPs and HGF pretreated cells at varying times. The red circle indicates endocytosed AuDNPs. Inset: enlarged image of the typical nanoparticles in cells. (B) The average MSD of AuDNPs in living cells after being incubated for different times. (C,D) Distributions of the α (B) and D_t (C) of AuDNPs in living cells after being incubated for different times. (E) The time series D_t of a single AuDNP extracted from the real-time DFM monitoring. (F) Schematic illustration of the endocytosis dynamics of AuDNPs. According to the characteristic dynamic of AuDNPs in cells at different times, the cellular uptake of AuDNPs was divided into two stages. Pause: captured and encapsulated by the nascent vesicles; Directional: diffused in the cytoplasm toward the nucleus, eventually confined in the crowded perinucleus. (G) TEM image of MDA-MB-231 cell after being treated with AuMNPs in the presence of HGF. Inset: the enlarged image in the red dashed box.

1003 after 1 h was mainly caused by the endocytosis of nanoparticle-bound Met into the cell. Notably, the nanoparticle-mediated endocytosis proceeded independently of Met activation, as evidenced by consistently low phosphorylation levels at the Y1234/5 site (Figure S44). After 1 h, Met expression continued to decrease with time, indicating that protein degradation was predominantly driven by the ongoing endocytosis of AuMNPs. Furthermore, Met degradation led to suppression of downstream signaling pathways, as demonstrated by significantly reduced cellular migration in both SL1 and AuMNP treatment groups compared to the controls (Figures S45−S48).

Observation of the Phosphorylated Met (p-Met) Degradation Process via Cellular Tracking of AuDNPs. Ligand-induced dimerization of Met receptors is critical for downstream cellular signaling, and different techniques have been proposed to investigate this essential process.[43,44] However, few nanoprobes are capable of specifically monitoring the endocytic trafficking of dimerized receptors. To address this limitation, we engineered plasmonic rulers (AuDNPs) by combining low-density modified AuNPs with proximity-induced DNA hybridization, enabling in situ detection of Met dimerization (Figure S49).[23] Through SPT (see experimental details in the Supporting Information), we explored the real-time dynamics of AuDNPs in living MDA-MB-231 cells at individual protein resolution. Time-resolved DFM imaging (Δt = 100 ms, acquisition duration = 60 s) revealed the dynamics of membrane-bound AuDNPs, which appeared as distinctive orange spots on the cell membrane (Figure 4A). Similar to AuMNPs targeting Met monomers, most dimerized proteins moved toward the nucleus over time. Spatiotemporal analysis through $X-Y$ trajectory mapping over 1 min intervals provided a detailed visualization of protein movement patterns (Figures S50−S52).

For quantitative analysis, we tracked approximately 40 independent trajectories per experimental group as a function of time lag (Δt) and performed mean MSD fitting analysis (Figure 4B). The endocytosis dynamics of Met dimers exhibited distinct patterns compared to monomers, which could be categorized into two main types: pause and directional transport (Figures S53−S56). Specifically, the motility of AuDNPs was found to be significantly confined

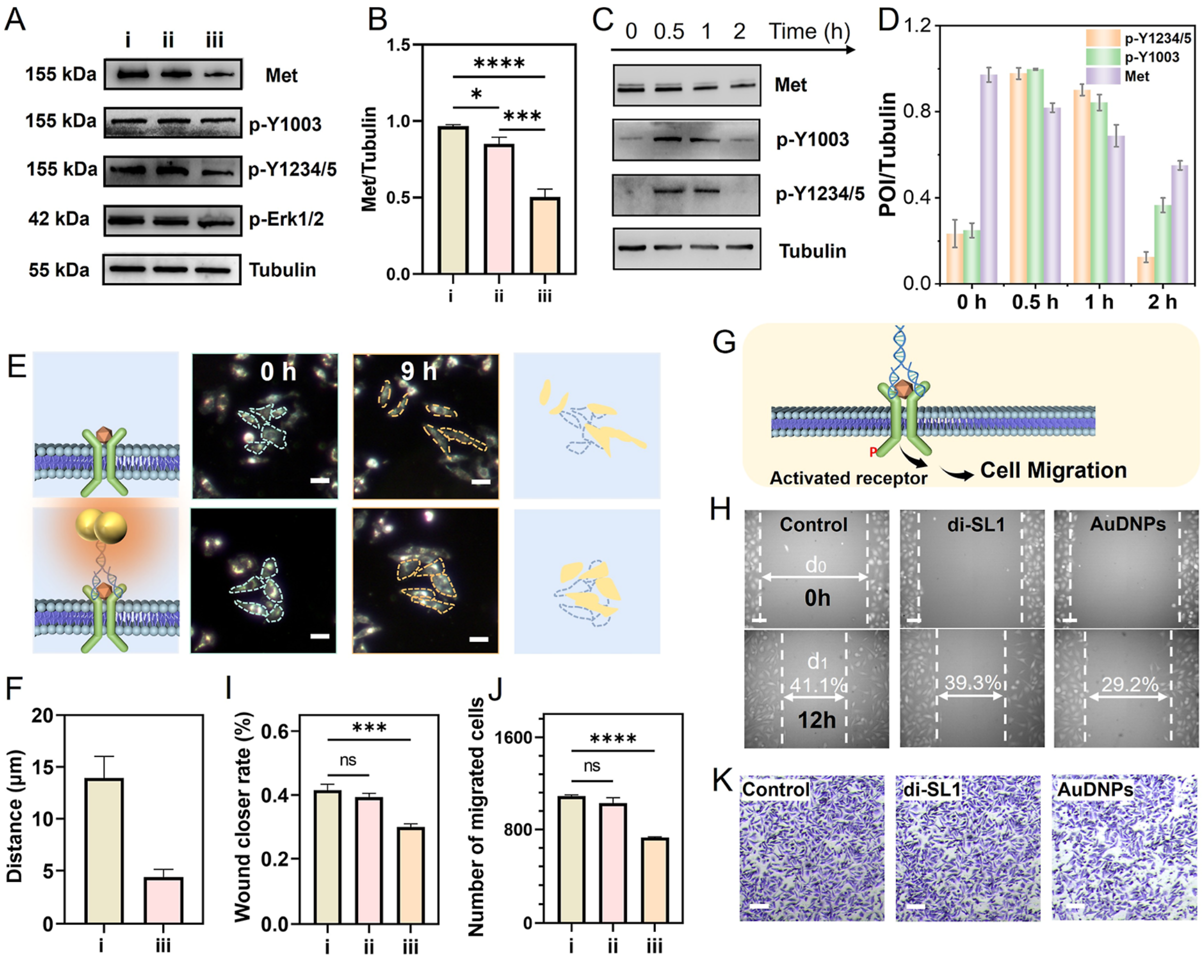

Figure 5. Analysis of the pathway and mechanism of p-Met degradation triggered by AuDNPs. (A) WB analysis of Met, Met phosphorylation, and Erk1/2 phosphorylation after different treatments [(i) control, (ii) di-SL1 treated, (iii) AuDNPs treated] in the presence of 100 ng/mL HGF. (B) Statistics of the level of Met after different treatments [(i) control, (ii) di-SL1 treated, (iii) AuDNPs treated] in the presence of 100 ng/mL HGF. (C) WB analysis of the level of Met and Met phosphorylation treated with AuDNPs after different times. (D) Statistics of the level of Met and p-Met after treatment with AuDNPs for different times. (E) DFM images of cell movement tracking in a 9 h interval and the comparison of migration before and after 9 h. Scale bar: 30 μm. (F) Statistics of the migration distance with (i) and without (ii) AuDNPs treatment. (G) Schematic illustration of the HGF-activated Met signaling. (H,I) Wound healing assay (H) and quantitative wound closure rate of cells (I) after different treatments [(i) control, (ii) di-SL1 treated, (iii) AuDNPs treated] in the presence of 100 ng/mL HGF. Scale bar:40 μm. (J,K) Statistical analysis of the cell counts (J) and the optical images (K) in the transwell migration assay after different treatments [(i) control, (ii) di-SL1 treated, (iii) AuDNPs treated] in the presence of 100 ng/mL HGF. Scale bar: 100 μm. The above data are presented as mean values ± SD ($n = 3$). Statistical significance was calculated by Student's t-test (unpaired, two-tailed): $^{*}p < 0.1$, $^{***}p < 0.001$, $^{****}P < 0.0001$.

for 15 min. The motility displacement, diffusion exponent ($\alpha \sim 0.164$), and diffusion coefficient ($D_t \sim 0.000243$) of AuDNPs were relatively low (Figure 4C,D). We attributed this restricted state to receptor-mediated endocytosis initiated by Met dimerization, which facilitated AuDNP transition into a confined state.[26] After 30 min, the displacement, α, D_t, and velocity of AuDNPs showed an increasing trend compared with the previous stage. This suggests that AuDNPs-Met dimer complexes had internalized and fused with early endosomes in the cell periphery, followed by cytoskeleton-mediated sorting to various cellular destinations.[13] The X−Y trajectories of AuDNPs demonstrated that the dimers no longer lingered in a severely restricted manner but began to move initially oriented toward the nuclear, with the average diffuse exponent increased above 0.352. Subsequently, the statistics of relative nanoparticle positions and trajectory data from SPT revealed that the motility of AuDNPs reaches a peak at 1 h. The increasing values of α and D_t also indicate that the confinement degree is relatively low at this stage, with a strong directionality of the motion. After 2 h of incubation, AuDNPs continued to move toward the nucleus under the wrapping of the endosomes. Their movement state still showed directional movement, but the movement directionality and diffusion index were weakened ($\alpha \sim 0.319$, $D_t \sim 0.000803$). Up to 4 h later, most of the AuDNPs appeared in the perinuclear area, at which point the degree of restriction increased and the AuDNP nanoprobes were almost "stagnant" (Figures S57 and S58).

Notably, the trajectories of AuDNPs in A549 cells were consistent with those observed in MDA-MB-231 cells, underscoring the generalizability of this responsive plasmonic probe for promoting as well as visualizing membrane protein degradation (Figure S59). To further support the above results, we conducted real-time tracking of individual AuDNP within single cells (Figure S60). As shown in Figure 4E, the temporal evolution of diffusion coefficients extracted from single-particle trajectories corroborated our observations of Met dimer dynamics on the MDA-MB-231 cell membranes, as described above. AuDNPs bound to the cell membrane

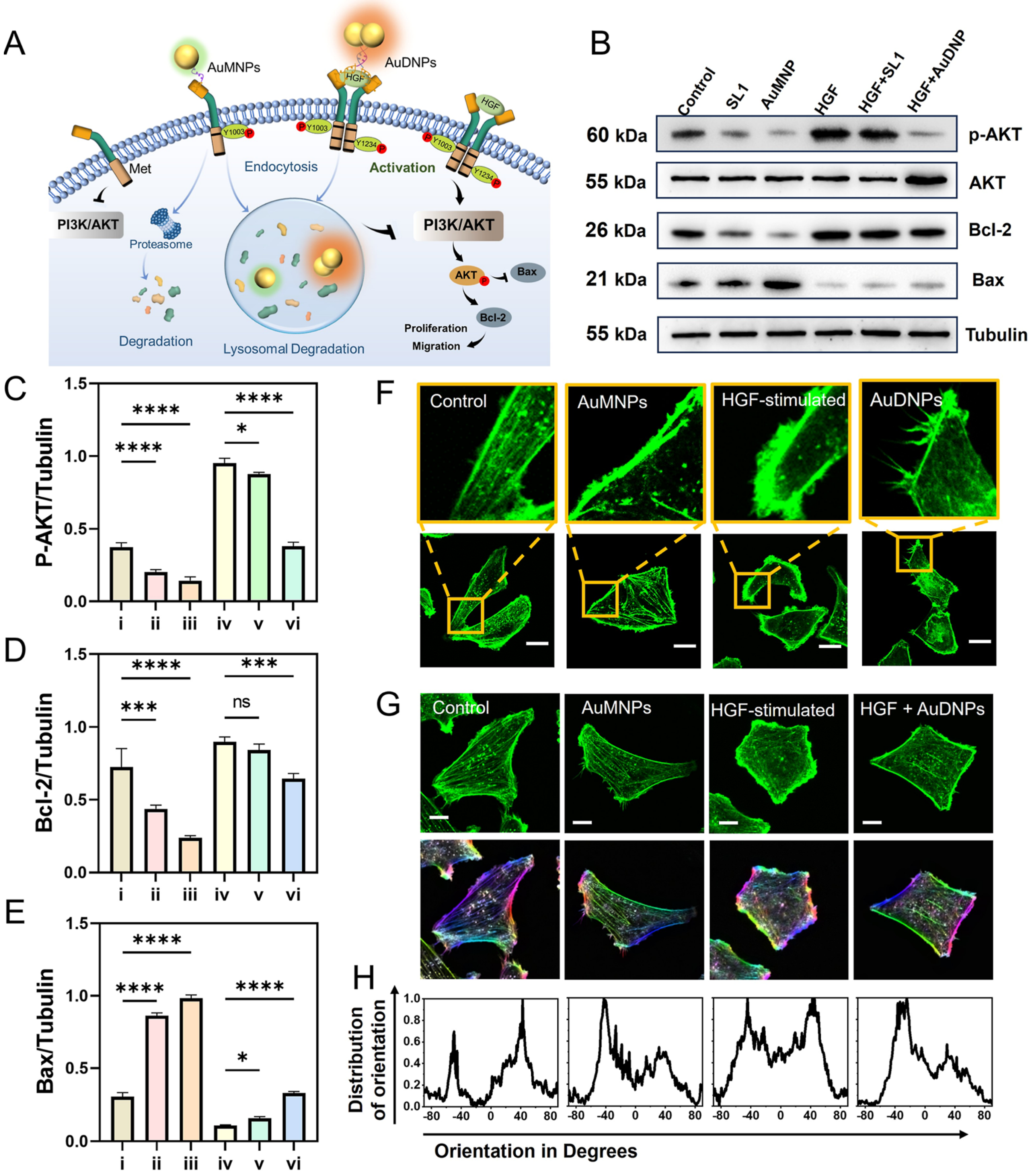

Figure 6. Effects of nanoparticle-mediated Met degradation on the PI3K/AKT signaling pathway. (A) Schematic illustration of how the nanoparticle-mediated Met degradation impairs the downstream kinase signal. (B) Immunoblotting analysis of relevant proteins after cells were treated with different conditions. (C−E) Quantitative analysis of *p*-Akt (C), Bcl-2 (D), and Bax (E) expression level by immunoblotting after treatment under different conditions [(i) control, (ii) SL1 treated, (iii) AuMNP treated, (iv) HGF treated, (v) HGF and di-SL1 treated, vi: HGF and AuDNPs treated]. Data are presented as mean ± SD ($n = 3$). Statistical significance was calculated by Student's *t*-test (unpaired, two-tailed): ns, no significant difference, $^{*}p < 0.05$; $^{***}p < 0.001$; $^{****}p < 0.0001$. (F−H) CLSM images of actin fibers (phalloidin staining) (F), the corresponding orientation of actin fibers highlighted with Orientation J (G), and the microdomain distributions for actin filament orientations (H) in MDA-MB-231 cells with different treatments.

appeared to be significantly restricted at ∼ 10 min, followed by endocytosis into the cell. After they underwent a period of directed movement, they were finally confined in the perinuclear area (Figure 4F). Moreover, the TEM results provided direct visualization of endosome-encapsulated AuDNPs during intracellular trafficking (Figure 4G).

To assess the contribution of nanoparticle size and shape to endocytosis, control dimers functionalized with nontargeting scrambled DNA (termed AuDNPs-RD) were synthesized. These exhibited scattering profiles similar to targeted AuDNPs (Figure S61A), but exhibited minimal cell binding and endocytosis due to a lack of targeting (Figure S61B). Another dimer probes targeting Met monomers (AuDNPs-m) were prepared via Met-targeted and untargeted strand hybridization, exhibiting morphological and optical properties comparable to those of AuDNPs (Figure S62), and bound effectively to MDA-MB-231 cells (Figure S61C). SPT revealed that AuDNPs-m exhibited motion patterns highly similar to those of monomeric AuMNPs, progressing through weakly confined, paused, and directional states (Figure S63), indicating that endocytic behaviors are primarily governed by the aggregation state of Met rather than the physical properties of the nanoparticles. Notably, rod-shaped nanoparticles with an aspect ratio of ∼2 (i.e., AuDNPs) are reported to exhibit slower cellular uptake compared to spherical counterparts.[45,46] Accordingly, the enhanced endocytosis observed here supports a biological mechanism whereby Met dimerization promotes clathrin-mediated internalization, rather than nonspecific physicochemical effects.[26]

Enhanced p-Met Degradation through the In Situ Assembly of AuDNPs. Previous studies have established that tyrosine kinase receptors initiate downstream signaling cascades upon ligand binding, concurrent with clathrin-mediated endocytosis.[9] Notably, elevated levels of activated RTKs are frequently observed in tumor tissues under physiological conditions.[47] However, the impact of nanoparticle-mediated protein endocytosis on preactivated target proteins remains largely unexplored. Under normal conditions, RTKs undergo internalization following ligand binding to activate downstream signaling pathways, with subsequent recycling to the cell membrane to maintain physiological activities.[26] Nevertheless, this process may be substantially disrupted due to the presence of nanoparticles. As displayed in Figure S48, immunofluorescence analysis revealed that the Met level on MDA-MB-231 cell membranes progressively decreased with time following treatment with AuMNPs and HGF. Consistent with this, when cells treated for 6 h were labeled with SL1-A-FAM, only a faint FAM fluorescence signal was detected (Figure S65). We hypothesized that Met dimers would be transported along with the conjugated AuDNPs via the endosomal-lysosomal pathway and trapped in the lysosome, resulting in enhanced lysosomal degradation of p-Met.

To verify this deduction, we first explored the expression and phosphorylation level of Met after the in situ assembly of AuDNPs on the cell membrane. As depicted in Figures 5A and S66, the addition of HGF significantly increased the phosphorylation level of intracellular structural domain Y1234/5 in Met, which is a key step in triggering the downstream signaling pathway. Notably, AuDNP treatment markedly attenuated Met level, an effect not observed with nonfunctionalized AuNPs (Figure S67). Meanwhile, the AuDNP-treated group displayed significantly lower intracellular Met expression after 1 h of incubation (Figure 5B). Whereas other membrane proteins, such as FGFR and epidermal growth factor receptor (EGFR), remained unaffected following treatment (Figure S68). These results suggested that AuDNPs could induce the degradation of p-Met. According to the WB analysis after treatment for different time periods, it was found that both p-Y1234/5 and p-Y1003 levels were highest at 0.5 and 1 h for dimerized Met (Figure 5C), coinciding with the period of enhanced AuDNP motility observed in trajectory analysis. After 2 h, a significant reduction in both Met and p-Met levels was observed (Figure 5D), which is consistent with trafficking to late endosomes and lysosomes and subsequent degradation. When evaluated by surface protein biotinylation (Figure S69), the surface level of Met also reduced significantly, indicating that endocytic recycling of Met was markedly inhibited by AuDNPs. Colocalization analysis further demonstrated high Pearson's correlation coefficients between Met and markers of early endosomes, late endosomes, and lysosomes across different incubation time points (Figure S70). Moreover, BafA1 strongly inhibited AuDNP-induced Met degradation, whereas MG132 also reduced the level of degradation but to a markedly lesser extent (Figure S71). This confirms that AuDNP-mediated Met degradation primarily relies on the lysosomal pathway, driven by accelerated endocytosis.

To further validate our hypothesis that AuDNP-mediated endocytosis promotes Met degradation, we examined both the downstream Met signaling and cellular behavior following various treatments. Apparently, in the presence of AuDNPs, the intracellular phosphorylation level of Erk1/2 was significantly reduced compared to HGF-treated groups (Figure 5C). As is known, the Met receptor activation triggers the Met signaling pathway and downstream signaling cascades, of which the promotion of cell migration is an important indication. To further validate the effect of nanoparticle-mediated p-Met endocytosis on cell motility, a live-cell tracking analysis was conducted using optical microscopy (Figure 5E and S72). As shown in Figure 5F, HGF-treated MDA-MB-231 cells exhibited visible migration after 9 h. The migration distance was significantly reduced after AuDNP treatment (Figure 5G). Similarly, as demonstrated in the wound healing assay, the migratory capacity of cells was significantly inhibited by treatment with AuDNPs (Figure 5H,I). Moreover, we conducted transwell assays to further reveal the influence of nanoparticle-induced p-Met degradation. The number of migrating cells of the AuDNP treatment was significantly lower than that of the only HGF treatment (Figures 5J and S73). The nonfunctionalized AuNPs or divalent aptamer binding induced minimal effect on the migration of MDA-MB-231 cells (Figures 5K and S74). All of these results supported the notion that the in situ assembly of AuDNPs could enhance p-Met degradation.

Nanoparticle-Mediated Met Degradation Impairs the Downstream Kinase Signal and Induces Cell Apoptosis. Met degradation led to reduced levels of phosphorylation, possibly impairing the Met signaling pathway (Figure 6A). Previous studies have established that Met activation promotes cell migration and proliferation while suppressing apoptosis through the PI3K/Akt pathway.[26] Accordingly, we further analyzed the expression and phosphorylation of relevant proteins in the Met downstream pathway, including Akt, phosphorylated Akt (*p*-Akt), antiapoptosis protein Bcl-2, and pro-apoptosis protein Bax. As displayed in Figure 6B, HGF treatment significantly elevated the levels of *p*-Akt and Bcl-2 compared to untreated controls, confirming ligand-dependent Met activation (Figure 6C,D). Notably, nanoparticle treatment markedly decreased Akt phosphorylation while substantially increasing Bax expression, even in Met-activated cells (Figure 6E).

Met/HGF signaling pathway promotes epithelial−mesenchymal transition upon activation, which is characterized by extensive spatiotemporal cytoskeletal remodeling.[48] To investigate cellular morphological changes, we visualized F-actin organization using FITC-phalloidin staining in MDA-MB-231 and A549 cells. Control cells exhibited a dense network of actin filaments along their periphery. After HGF stimulation, the cells extended the broad leading lamellipodium at the leading edge and spike-like filopodia at the cell periphery (Figures 6F and S75). AuDNP treatment significantly suppressed HGF-induced formation of lamellipodia and membrane ruffles. Additionally, the single-cell analysis was further performed to evaluate action fiber orientation and anisotropy of cells treated with AuMDPs or AuDNPs following the HGF treatment. Consistent with the decreased cell motility, the degradation of the Met monomer and dimer affected fiber orientation and anisotropy. The orientation maps of cytoskeletal structures were generated by ImageJ, where the same color represents the same orientation (Figure S76). As opposed to the monotonous colors shown in the control group, intracellular actin exhibited colored orientation maps upon HGF stimulation, demonstrating the successful activation of cytoskeletal reorganization by HGF. In contrast, AuDNP-treated cells maintained relatively monotonous coloration despite HGF activation, suggesting the effective inhibition of HGF-dependent cytoskeletal rearrangement (Figures 6G, S77, and S78). Moreover, the anisotropy values of the cells in the nanoparticle-treated group were significantly higher than those of the cells in the HGF-treated group (Figure 6H). These results revealed that nanoparticle-induced Met degradation disrupts the cytoskeletal rearrangement, thereby inhibiting cancer cell mobility. Furthermore, the effect of AuMNPs and AuDNP-mediated Met degradation on cell apoptosis in MDA-MB-231 cells was investigated. As shown in Figure S79, the cell viability analysis indicated that nanoparticle-treated cells significantly affected the viability, which was further decreased with the prolongation of incubation time. Taken together, Met degradation triggered by aptamer-modified nanoparticles could surmount the signal activation of Met in the presence of HGF, thereby suppressing Met signal transduction and triggering cell apoptosis.

To demonstrate the broad applicability of the proposed membrane protein degradation platform, we further applied it to EGFR, another receptor tyrosine kinase commonly overexpressed in cancers.[49] Using EGFR-specific aptamers (EGFR-S1 and EGFR-S2, Table S1), we constructed corresponding nanoprobes (AuMNPs-E and AuDNPs-E) following the same procedure as that for Met-targeting probes. As shown in Figure S80, both AuMNPs-E and AuDNPs-E significantly reduced EGFR expression levels, indicating effective degradation of EGFR. We further evaluated downstream signaling events and found that nanoparticle treatment suppressed EGF-induced Akt phosphorylation and increased Bax expression (Figure S81). Moreover, FITC-phalloidin staining of F-actin revealed that EGFR degradation disrupted the cytoskeletal organization. AuDNPs-E-treated cells showed homogeneous F-actin distribution even after EGF stimulation, suggesting inhibition of EGF-dependent cytoskeletal remodeling (Figure S82). These results collectively demonstrate that the proposed platform provides a versatile and generalizable strategy for the targeted degradation of diverse membrane proteins.

CONCLUSION

In summary, we have developed a responsive plasmonic nanoprobe system that precisely distinguished membrane protein monomers from dimers, enabling the real-time monitoring of protein degradation dynamics in different aggregate states through nanoparticle endocytosis. The nanoprobes, featuring precisely controlled low-density aptamer modifications, can engage with individual proteins via a low-valency binding mode. When natural ligands induce proteins into a dimerized state, nanoprobes bound to Met form dimer structures through proximity-induced DNA hybridization, generating distinct plasmon coupling signals. Taking Met protein as a model system, we demonstrated differential endocytosis kinetics between monomeric and dimeric states, with the latter showing an enhanced internalization efficiency. Furthermore, comprehensive mechanistic studies uncovered aggregate-state-dependent p-Met degradation efficiencies and associated cellular responses. Noteworthily, benefiting from the well-established aptamer screening technologies and extensive aptamer libraries, this nanoprobe system can be easily adapted to the study of the internalization and degradation process of other membrane receptors (e.g., VEGFR2 and HER2). Looking forward, rapid advances in nanotechnology and microscopic imaging are expected to further refine this platform, enabling more precise control over stoichiometric modification and reduced nanoscale steric interference. These improvements will facilitate a comprehensive, single-molecule-level perspective of how protein aggregation states guide the design and optimization of TPD platforms. This work provides nanoscale insights into receptor endocytosis dynamics while establishing a versatile platform for cellular uptake modulation and TPD with broad implications for therapeutic development and fundamental cell biology research.

ASSOCIATED CONTENT

Supporting Information

The Supporting Information is available free of charge at https://pubs.acs.org/doi/10.1021/jacs.5c12343.

Details of reagents and apparatus, methods, and supplementary experimental data (PDF)

AUTHOR INFORMATION

Corresponding Author

Chen Wang − *State Key Laboratory of Microbial Technology, Jiangsu Collaborative Innovation Center of Biomedical Functional Materials, School of Chemistry and Materials Science, Nanjing Normal University, Nanjing 210023, China;* orcid.org/0000-0001-6544-4065; Email: wangchen@njnu.edu.cn

Authors

Jin Wang − *State Key Laboratory of Microbial Technology, Jiangsu Collaborative Innovation Center of Biomedical Functional Materials, School of Chemistry and Materials Science, Nanjing Normal University, Nanjing 210023, China;* orcid.org/0000-0003-4525-9924

Jing Tan − *State Key Laboratory of Microbial Technology, Jiangsu Collaborative Innovation Center of Biomedical Functional Materials, School of Chemistry and Materials Science, Nanjing Normal University, Nanjing 210023, China*

Zhao Zhang − *State Key Laboratory of Microbial Technology, Jiangsu Collaborative Innovation Center of Biomedical Functional Materials, School of Chemistry and Materials Science, Nanjing Normal University, Nanjing 210023, China*

Xiuxiu Wang − *State Key Laboratory of Coordination Chemistry, Chemistry and Biomedicine Innovation Center (ChemBIC), School of Chemistry and Chemical Engineering, Nanjing University, Nanjing 210093, China*

Jing Zhao − *State Key Laboratory of Coordination Chemistry, Chemistry and Biomedicine Innovation Center (ChemBIC), School of Chemistry and Chemical Engineering, Nanjing University, Nanjing 210093, China;* orcid.org/0000-0001-5177-5699

Jie Li − *Department of Oncology, Guang' Anmen Hospital, China Academy of Chinese Medical Sciences, Beijing 100053, China;* orcid.org/0000-0002-0952-093X

Complete contact information is available at: https://pubs.acs.org/10.1021/jacs.5c12343

Notes

The authors declare no competing financial interest.

■ ACKNOWLEDGMENTS

This work was supported by grants from the National Key Research and Development Program of China (No. 2025YFC3409400), the National Natural Science Foundation of China (22274076, 22304084), the Natural Science Foundation of Jiangsu Province (BK20230377), and Jiangsu Provincial Department of Education (211090B52303).

■ REFERENCES

(1) Zhang, D.; Duque-Jimenez, J.; Facchinetti, F.; Brixi, G.; Rhee, K.; Feng, W. W.; Jänne, P. A.; Zhou, X. Transferrin receptor targeting chimeras for membrane protein degradation. *Nature* **2025**, *638*, 787−795.

(2) Zhao, L.; Zhao, J.; Zhong, K.; Tong, A.; Jia, D. Targeted protein degradation: mechanisms, strategies and application. *Signal Transduction Targeted Ther.* **2022**, *7* (1), 113.

(3) Hsia, O.; Hinterndorfer, M.; Cowan, A. D.; Iso, K.; Ishida, T.; Sundaramoorthy, R.; Nakasone, M. A.; Imrichova, H.; Schätz, C.; Rukavina, A.; Husnjak, K.; Wegner, M.; Correa-Sáez, A.; Craigon, C.; Casement, R.; Maniaci, C.; Testa, A.; Kaulich, M.; Dikic, I.; Winter, G. E.; Ciulli, A. Targeted protein degradation via intramolecular bivalent glues. *Nature* **2024**, *627* (8002), 204−211.

(4) Baker, A. G.; Ho, A. P. T.; Itzhaki, L. S.; Fruk, L. Nanoparticle-Mediated Targeted Protein Degradation: An Emerging Therapeutics Technology. *Angew. Chem., Int. Ed.* **2025**, *64* (28), No. e202503958.

(5) Ahn, G.; Riley, N. M.; Kamber, R. A.; Wisnovsky, S.; Moncayo von Hase, S.; Bassik, M. C.; Banik, S. M.; Bertozzi, C. R. Elucidating the cellular determinants of targeted membrane protein degradation by lysosome-targeting chimeras. *Science* **2023**, *382* (6668), No. eadf6249.

(6) Wang, Q.; Yang, X.; Yuan, R.; Shen, A.; Wang, P.; Li, H.; Zhang, J.; Tian, C.; Jiang, Z.; Li, W.; Dong, S. A co-assembly platform engaging macrophage scavenger receptor A for lysosome-targeting protein degradation. *Nat. Commun.* **2024**, *15* (1), 1663.

(7) Ahn, G.; Banik, S. M.; Miller, C. L.; Riley, N. M.; Cochran, J. R.; Bertozzi, C. R. LYTACs that engage the asialoglycoprotein receptor for targeted protein degradation. *Nat. Chem. Biol.* **2021**, *17* (9), 937−946.

(8) Cui, M.; Zhang, D.; Zheng, X.; Zhai, H.; Xie, M.; Fan, Q.; Wang, L.; Fan, C.; Chao, J. Intelligent Modular DNA Lysosome-Targeting Chimera Nanodevice for Precision Tumor Therapy. *J. Am. Chem. Soc.* **2024**, *146* (43), 29609−29620.

(9) Banushi, B.; Joseph, S. R.; Lum, B.; Lee, J. J.; Simpson, F. Endocytosis in cancer and cancer therapy. *Nat. Rev. Cancer* **2023**, *23* (7), 450−473.

(10) Fan, Z.; Mao, X.; Zhu, M.; Hu, X.; Li, M.; Huang, L.; Li, J.; Maimaiti, T.; Zuo, X.; Fan, C.; Li, Q.; Liu, M.; Tian, Y. Probing Twist-Induced Endocytotic Membrane Fission using Anisotropic Gold Homodimers. *Angew. Chem., Int. Ed.* **2024**, *64*, No. e202413244.

(11) Ma, W.; Zhan, Y.; Zhang, Y.; Shao, X.; Xie, X.; Mao, C.; Cui, W.; Li, Q.; Shi, J.; Li, J.; Fan, C.; Lin, Y. An Intelligent DNA Nanorobot with in Vitro Enhanced Protein Lysosomal Degradation of HER2. *Nano Lett.* **2019**, *19* (7), 4505−4517.

(12) Rennick, J. J.; Johnston, A. P. R.; Parton, R. G. Key principles and methods for studying the endocytosis of biological and nanoparticle therapeutics. *Nat. Nanotechnol.* **2021**, *16* (3), 266−276.

(13) Liu, M.; Wang, F.; Zhang, X.; Mao, X.; Wang, L.; Tian, Y.; Fan, C.; Li, Q. Tracking endocytosis and intracellular distribution of spherical nucleic acids with correlative single-cell imaging. *Nat. Protoc.* **2021**, *16* (1), 383−404.

(14) Liu, Y.; Liu, R.; Dong, J.; Xia, X.; Yang, H.; Wei, S.; Fan, L.; Fang, M.; Zou, Y.; Zheng, M.; Leong, K. W.; Shi, B. Targeted protein degradation via cellular trafficking of nanoparticles. *Nat. Nanotechnol.* **2025**, *20*, 296−302.

(15) Liu, R.; Yun, Y.; Feng, Z.-Y.; Feng, Z.; Zhang, W.; Ye, Y.; Zhang, J. Customizable Aptamer-Engineered Nano-Lysosome-Targeting Chimeras Enable Receptor-Independent and High-Fidelity Degradation of Membrane Protein. *CCS Chem.* **2025**, 1.

(16) Sun, W.; Zhang, H.; Xie, W.; Ma, L.; Dang, Y.; Liu, Y.; Li, L.; Qu, F.; Tan, W. Development of Integrin-Facilitated Bispecific Aptamer Chimeras for Membrane Protein Degradation. *J. Am. Chem. Soc.* **2024**, *146* (37), 25490−25500.

(17) Huang, L.; Mao, X.; Li, J.; Li, Q.; Shen, J.; Liu, M.; Fan, C.; Tian, Y. Nanoparticle Spikes Enhance Cellular Uptake via Regulating Myosin IIA Recruitment. *ACS Nano* **2023**, *17* (10), 9155−9166.

(18) Wen, X.; Sang, Y.; Zhang, Y.; Ge, F.; Jing, G.; He, Y. Direct Observation of Nanotracer Transport in Swarming Bacteria during Antibiotic Adaptation. *ACS Nano* **2023**, *17* (11), 10104−10112.

(19) Xiong, B.; Wu, J.; Shang, J.; Chen, Y.; He, Y.; Zhang, X.-B.; Tan, W. Probing Allosteric Modulation of Membrane Receptor in the Native State by Data Mining-Integrated Tracking Microscopy. *CCS Chem.* **2022**, *4* (9), 3150−3161.

(20) Wang, J.; Yu, Q.; Li, X.-L.; Zhao, X.-L.; Chen, H.-Y.; Xu, J.-J. A reversible plasmonic nanoprobe for dynamic imaging of intracellular pH during endocytosis. *Chem. Sci.* **2022**, *13* (17), 4893−4901.

(21) Wang, J.; Wang, C.; Xu, J.-J.; Xia, X.-H.; Chen, H.-Y. Emerging advances in plasmonic nanoassemblies for biosensing and cell imaging. *Chin. Chem. Lett.* **2023**, *34* (9), 108165.

(22) Wang, S.-M.; Wang, H.; Gao, H.; Zhou, J.; Zhao, W.; Chen, H.-Y.; Xu, J.-J. Single-Particle Plasmonic Sensing of Nitric Oxide in Living Cells. *Anal. Chem.* **2023**, *95* (17), 7062−7069.

(23) Wang, J.; Song, J.; Zhang, X.; Wang, S.-M.; Kang, B.; Li, X.-L.; Chen, H.-Y.; Xu, J.-J. DNA-Programed Plasmon Rulers Decrypt Single-Receptor Dimerization on Cell Membrane. *J. Am. Chem. Soc.* **2023**, *145* (2), 1273−1284.

(24) Ye, Z.; Zhang, C.; Yuan, J.; Xiao, L. Ligand−Receptor Interaction Triggers Hopping and Sliding Motions on Living Cell Membranes. *J. Am. Chem. Soc.* **2023**, *145* (46), 25177−25185.

(25) Ge, F.; Du, Y.; He, Y. Direct Observation of Endocytosis Dynamics of Anti-ErbB Modified Single Nanocargoes. *ACS Nano* **2022**, *16* (4), 5325−5334.

(26) Ménard, L.; Parker, P. J.; Kermorgant, S. Receptor tyrosine kinase c-Met controls the cytoskeleton from different endosomes via different pathways. *Nat. Commun.* **2014**, *5* (1), 3907.

(27) Walker, G.; Brown, C.; Ge, X.; Kumar, S.; Muzumdar, M. D.; Gupta, K.; Bhattacharyya, M. Oligomeric organization of membrane proteins from native membranes at nanoscale spatial and single-molecule resolution. *Nat. Nanotechnol.* **2024**, *19* (1), 85−94.

(28) Sigismund, S.; Lanzetti, L.; Scita, G.; Di Fiore, P. P. Endocytosis in the context-dependent regulation of individual and collective cell properties. *Nat. Rev. Mol. Cell Biol.* **2021**, *22* (9), 625−643.

(29) He, F.; Wang, M.; Wang, J.; Wang, H.-H.; Nie, Z. An Extracellular miRNA-Responsive Artificial Receptor via Dynamic DNA Nano-assembly for Biomarker-Driven Therapy. *Angew. Chem., Int. Ed.* **2023**, *62* (31), No. e202305227.

(30) Chen, Y.; Morihiro, K.; Nemoto, Y.; Ichimura, A.; Ueki, R.; Sando, S.; Okamoto, A. Selective inhibition of cancer cell migration using a pH-responsive nucleobase-modified DNA aptamer. *Chem. Sci.* **2024**, *15* (41), 17097−17102.

(31) Ueki, R.; Ueki, A.; Kanda, N.; Sando, S. Oligonucleotide-Based Mimetics of Hepatocyte Growth Factor. *Angew. Chem., Int. Ed.* **2016**, *55* (2), 579−582.

(32) Liang, H.; Chen, S.; Li, P.; Wang, L.; Li, J.; Li, J.; Yang, H.-H.; Tan, W. Nongenetic Approach for Imaging Protein Dimerization by Aptamer Recognition and Proximity-Induced DNA Assembly. *J. Am. Chem. Soc.* **2018**, *140* (12), 4186−4190.

(33) Chen, X.; Wang, Y.; Dai, X.; Ding, L.; Chen, J.; Yao, G.; Liu, X.; Luo, S.; Shi, J.; Wang, L.; Nechushtai, R.; Pikarsky, E.; Willner, I.; Fan, C.; Li, J. Single-Stranded DNA-Encoded Gold Nanoparticle Clusters as Programmable Enzyme Equivalents. *J. Am. Chem. Soc.* **2022**, *144* (14), 6311−6320.

(34) Hao, C.; Meng, D.; Shi, W.; Xu, C.; Wang, Q.; Kuang, H. Chiral Gold Nanostructure Monolayers as SERS Substrates for Ultrasensitive Detection of Enantiomer Biomarkers of Alzheimer's Disease. *Angew. Chem., Int. Ed.* **2025**, *64* (21), No. e202502115.

(35) Li, X.-L.; Zhang, Z.-L.; Zhao, W.; Xia, X.-H.; Xu, J.-J.; Chen, H.-Y. Oriented assembly of invisible probes: towards single mRNA imaging in living cells. *Chem. Sci.* **2016**, *7* (5), 3256−3263.

(36) Salarvand, A.; Shanei, A.; Hejazi, S. H.; Kakhki, N. A.; Abharian, P. H.; Najafizade, N. In Vitro Study of Sonodynamic Therapy Using Gemcitabine-Loaded PEG-Gold Nanoparticles Against MCF-7 Breast Cancer Cells. *BioNanoSci.* **2024**, *14* (3), 2117−2130.

(37) Ye, Z.; Liu, H.; Wang, F.; Wang, X.; Wei, L.; Xiao, L. Single-particle tracking discloses binding-mediated rocking diffusion of rod-shaped biological particles on lipid membranes. *Chem. Sci.* **2019**, *10* (5), 1351−1359.

(38) Liu, M.; Li, Q.; Liang, L.; Li, J.; Wang, K.; Li, J.; Lv, M.; Chen, N.; Song, H.; Lee, J.; Shi, J.; Wang, L.; Lal, R.; Fan, C. Real-time visualization of clustering and intracellular transport of gold nanoparticles by correlative imaging. *Nat. Commun.* **2017**, *8* (1), 15646.

(39) Chen, K.; Cai, J.; Wang, S.; Li, Y.; Yang, C.; Fu, T.; Zhao, Z.; Zhang, X.; Tan, W. Aptamer Inhibits Tumor Growth by Leveraging Cellular Proteasomal Degradation System to Degrade c-Met in Mice. *Angew. Chem., Int. Ed.* **2022**, *62* (2), No. e202208451.

(40) Ikemoto, M.; Furuchi, T.; Arai, H.; Inoue, K. Dual Pathways for the Secretion of Lysosomal Cholesterol into a Medium from Cultured Macrophages. *J. Biol. Chem.* **2000**, *128* (2), 251−259.

(41) Goldberg, A. L. Development of proteasome inhibitors as research tools and cancer drugs. *J. Cell Biol.* **2012**, *199* (4), 583−588.

(42) Ueki, R.; Atsuta, S.; Ueki, A.; Hoshiyama, J.; Li, J.; Hayashi, Y.; Sando, S. DNA aptamer assemblies as fibroblast growth factor mimics and their application in stem cell culture. *Chem. Commun.* **2019**, *55* (18), 2672−2675.

(43) Wang, M.; Yang, D.; Lu, Q.; Liu, L.; Cai, Z.; Wang, Y.; Wang, H.-H.; Wang, P.; Nie, Z. Spatially Reprogramed Receptor Organization to Switch Cell Behavior Using a DNA Origami-Templated Aptamer Nanoarray. *Nano Lett.* **2022**, *22* (21), 8445−8454.

(44) Wu, Y.; Huang, J.; He, H.; Wang, M.; Yin, G.; Qi, L.; He, X.; Wang, H.-H.; Wang, K. Logic Nanodevice-Mediated Receptor Assembly for Nongenetic Regulation of Cell Behavior in Tumor-like Microenvironment. *Nano Lett.* **2023**, *23* (5), 1801−1809.

(45) Chithrani, B. D.; Ghazani, A. A.; Chan, W. C. W. Determining the Size and Shape Dependence of Gold Nanoparticle Uptake into Mammalian Cells. *Nano Lett.* **2006**, *6* (4), 662−668.

(46) Huang, C.; Zhang, Y.; Yuan, H.; Gao, H.; Zhang, S. Role of Nanoparticle Geometry in Endocytosis: Laying Down to Stand Up. *Nano Lett.* **2013**, *13* (9), 4546−4550.

(47) Li, Y.; Arghittu, S. M.; Dietz, M. S.; Hella, G. J.; Haße, D.; Ferraris, D. M.; Freund, P.; Barth, H.-D.; Iamele, L.; de Jonge, H.; Niemann, H. H.; Covino, R.; Heilemann, M. Single-molecule imaging and molecular dynamics simulations reveal early activation of the MET receptor in cells. *Nat. Commun.* **2024**, *15* (1), 9486.

(48) Li, H.; Gao, J.; Cao, L.; Xie, X.; Fan, J.; Wang, H.; Wang, H. H.; Nie, Z. A DNA molecular robot that autonomously walks on the cell membrane to drive cell motility. *Angew. Chem., Int. Ed.* **2021**, *60* (50), 26291−26299.

(49) Xu, M. J.; Johnson, D. E.; Grandis, J. R. EGFR-targeted therapies in the post-genomic era. *Cancer Metastasis Rev.* **2017**, *36* (3), 463−473.